Facet-dependent interfacial charge separation and transfer in plasmonic photocatalysts

Jieyuan Li[a,b,1], Xing'an Dong[b,1], Yanjuan Sun[b], Wanglai Cen[a,*], Fan Dong[b,*]

[a] College of Architecture and Environment, Institute of New Energy and Low Carbon Technology, Sichuan University, Chengdu, Sichuan 610065, PR China
[b] Chongqing Key Laboratory of Catalysis and New Environmental Materials, College of Environment and Resources, Chongqing Technology and Business University, Chongqing 400067, PR China

ABSTRACT

Surface plasmon resonance (SPR) induced plasmonic photocatalysis provides a brand new way for more efficient light absorption and utilization to achieve better solar light conversion. Although the SPR effect in metal-semiconductor photocatalysis has been widely investigated, the SPR-driven interfacial charge separation and transfer patterns between the two counterparts have not yet been fully revealed. The plasmonic metal-semiconductor photocatalytic systems require to be rationally designed, especially for the facet-aspect of the semiconductor, which can dominantly endow the contacting interface with diverse charge transfer patterns. Taken Bi metal deposited at the typical (001) and (010) facets of BiOBr nanosheets as a case study, we demonstrate that the surface charge alternation on the (010) facet highly favors the interfacial charge separation and transfer, by providing a new route of $[Bi_2O_2]^{2+} \rightarrow$ plasmonic metal $\rightarrow Br^-$ for interfacial carriers transfer. The charge alternation on discrepant semiconductor facets in essence makes the plasmonic photocatalytic system be different in charge transportation pattern. These new findings are further validated in extensive composite systems composed of alternative plasmonic metal (Ag and Au) and semiconductors (BiOCl and BiOI). The perspective here can open numerous possibilities for the rational design of more efficient plasmonic photocatalysts.

1. Introduction

Surface plasmon resonance (SPR), originating from the strong light absorption and collective electron oscillation of specific metals, has recently become an appealing research spot, and been widely studied for efficient solar light conversion.[1–5] Under light irradiation, the SPR induced hot carriers can be injected into the adjacent semiconductor support for various reactions, such as pollutants degradation, reactive oxygen species (ROS) generation and water spitting.[6–10] In a typical plasmonic metal-semiconductor photocatalytic system, the contacting interface, which essentially provides the transfer tunnel for the hot carriers' migration, is of crucial importance.[11–14] The patterns of the interfacial charge separation and transfer should be tightly controlled to further functionalize the plasmonic photocatalysts. Recently, various advances have been proposed to promote the efficiency of interfacial charge transfer, mainly by means of foreign elemental doping, defect construction and facet engineering.[15–19] Therein, facet engineering should be the prerequisite to be considered, because the surface atomic arrangements dominantly endow the contacting interface with diverse charge transfer patterns, hence affecting the light

absorption and charge transfer efficiency, and subsequently tuning the photocatalytic activity and selectivity.[20–24]

BiOX (X = Cl, Br and I), with $[Bi_2O_2]^{2+}$ slabs sandwiched in double halide anion layers, has ignited enormous research interests in photocatalysis, due to its fascinating and tunable nanostructure on different facets.[25–28] The intrinsic layered structures build the internal electronic field for charge transfer from $[Bi_2O_2]^{2+}$ to halide anions. It is worth noting that the charge travelling length and direction are quite different on the orthogonal (001) and (010) facets. By the contribution of the bulk charge alternation (BCA) and surface charge alternation (SCA) on the respective (001) and (010) facets, the electrons can transfer within the (001) bulk, but along the (010) surface.[29–32] These distinct charge transfer patterns conclusively make the interface be different when BiOX is chosen as a support for plasmonic photocatalysts. The facet-dependent interfacial charge separation and transfer pattern is vital for understanding and manipulating the interface design to enhance plasmonic photocatalysis, however, which has not been reported.

Herein, taken Bi metal deposited BiOBr nanosheets (Bi-BiOBr) with the exposure of respective (001) and (010) facets as a case study, the

interfacial charge separation and transfer pattern of plasmonic photocatalysts is firstly revealed, which directly indicates that the (010) facet of BiOBr preferably enhances the interfacial charge separation, thus resulting in the reinforced plasmonic photocatalysis for NO removal owing to the SCA. Except for the SPR effect of Bi element that enables hot carriers to transfer from the plasmonic metal to BiOBr, we demonstrate an additional electron transfer channel along the path of $[Bi_2O_2]^{2+} \rightarrow$ plasmonic metal $\rightarrow Br^-$ at (010) facet of BiOBr (Bi-010), also supported by DFT calculations. The inherent SCA on (010) facet can result in more efficient inhibition of the interfacial electron-hole recombination than that of the (001) facet (Bi-001). The experimental results further certify the theoretical design that the plasmonic photocatalysis efficiency of Bi@010 significantly exceeds that of Bi@001 due to the reinforced interfacial charge separation and transfer pattern.

Our conclusions are further verified in extensive metal-semiconductor systems composed of alternative plasmonic metal (Ag and Au) and semiconductors (BiOCl and BiOI). The results demonstrate that the charge alternation on discrepant semiconductor facets conclusively makes the plasmonic photocatalytic system be different in charge transportation pattern, leading to distinct promotion mechanism for photocatalytic NO removal. The particular SCA is dominantly responsible for the highly accelerated interfacial charge separation, resulting in the significantly reinforced plasmonic photocatalysis. This work provides a facet-dependent protocol for the novel design of highly efficient plasmonic photocatalysts, and paves a new way to investigate the underlying mechanism. The perspective here could deepen the understanding of general facet effect and broaden its utilization in the vast fields of environmental and energy science.

2. Experimental section

2.1. Theoretical calculations

All the spin-polarized DFT-D2 calculations were conducted in the "Vienna ab initio simulation package" (VASP code 5.4.1), using the generalized gradient correlation functional.[33] The projector-augmented wave method was used with a plane-wave basis.[34] The cutoff energy and Gaussian smearing width were respectively set to 500 eV and 0.2 eV. The Brillouin zone was sampled with a $5 \times 5 \times 1$ K points. All structures and energy are allowed to relax below 0.01 eV Å^{-1}.

The simulation of the electromagnetic field distribution around Bi metal was performed with a rigorous Maxwell solver based on the finite integration techniques.[35,36] The refractive index of Bi element in the UV to near-infrared spectra was fitted to the Drude model of the empirical data.

2.2. Synthesis of photocatalysts

All chemicals used in this study were analytical grade (Sigma Aldrich) without further purification. 001 sample of BiOBr was synthesized using a modification of a reported protocol. In a typical measurement of synthesis, 2 mmol of $Bi(NO_3)_3 \cdot 5H_2O$ and 2 mmol of KBr were added to 60 mL distilled water at room temperature with continuous stirring. As for the (010) facet, 5 M NaOH solution was injected to this mixture in order to adjust its pH value to 6.0. The mixture was stirred for 30 min, and then moved into a 100 mL Teflon lined stainless autoclave to perform a hydrothermal process at 160 °C for 24 h. The resultant precipitates was then collected and washed thoroughly with deionized water and ethanol respectively for 3 times.

BiOBr with Bi nanowires deposited was prepared by an in situ reduction reaction. Typically, 2 mmol of BiOBr was added into 100 mL of deionized water containing 1.0 g PVP (polyvinyl pyrrolidone) and stirred for 20 min. Then a certain concentration of $NaBH_4$ (30 mL) was dropwise added into this solution under stirring and the mixture was further aged. The resultant precipitates were gathered and washed. When the concentration of $NaBH_4$ was 30, 50, 70 and 90 mmol L^{-1},

using 001 as precursor material, the obtained samples were denoted as 001–30, 001-50, 001-70 and 001-90, respectively. While for 010, the obtained samples were labeled as 010-30, 010-50, 010-70 and 010-90, respectively.

2.3. Characterizations

The X-ray diffraction (XRD) with Cu Kα radiation (model D/max RA, Rigaku Co. Japan) was utilized to analyze the crystal phases of the samples. The surface properties were investigated using the X-ray photoelectron spectroscopy (XPS) with Al Kα X-rays (Thermo ESCALAB 250, USA). The morphologies were examined with scanning electron microscopy (SEM, model JSM-6490, JEOL, Japan) and transmission electron microscopy, JEM-2010, Japan). A scanning UV–vis spectraphotometer (TU-1901, China) equipped with an integrating sphere was used to characterize the UV–vis diffuse reflectance spectrometry. Time-resolved fluorescence emission spectra were measured using a fluorescence spectrophotometer (Edinburgh Instruments, FLSP-920) at room temperature. The surface photovoltage (SPV) measurement was carried out on the basis of the lock-in amplifier.[37] The measurement system consists of a source of monochromatic light, a lock-in amplifier (SR830, Stanford Research Systems, Inc.) with a light chopper (SR540, Stanford Research Systems, Inc.) r. The monochromatic light is provided by passing light from a 500 W Xenon lamp (CHFXQ500 W, Global Xenon Lamp Power) though a grating monochromator (Omni-5007, No.09010, Zolix). The electron paramagnetic resonance (EPR) characterization (FLsp920, England) of the as-prepared photocatalysts was carried out at 77 K. Electron spin resonance (ESR) spectra of chemical radicals were obtained on a JES FA200 spectrometer to determine the involvement of the reactive oxygen species (ROS), respectively in methanol dispersion for DMPO-·O_2^- and in aqueous dispersion for DMPO-·OH.

2.4. Photocatalytic efficiency evaluation

The photocatalytic activities were investigated via the removal ratio of NO at ppb levels in a continuous-flow reactor (Scheme S1). A 150 W commercial tungsten halogen lamp was vertically placed outside the reactor. A UV cutoff filter (420 nm) was utilized to remove UV light in the light beam. For each test, 0.20 g of as-prepared sample was dispersed in distilled water (50 mL) in a beaker.

The NO gas was obtained from a compressed gas cylinder, and the concentration of NO was diluted to about 500 ppb by the air stream. The desired relative humidity level of the NO flow was controlled at 50% by passing the zero air streams through a humidification chamber. The gas streams were premixed completely using a gas blender. After adsorption–desorption equilibrium was achieved, the lamp was turned on. The concentration of NO was continuously measured using a NO_X analyzer (Thermo Environmental Instruments Inc., model 42c-TL). The removal ratio (η) of NO was defined as

$$\eta \ (\%) = (1 - C/C_0) \times 100\% \tag{1}$$

where C and C_0 stand for the concentrations of NO in the outlet and feeding stream, respectively.

Refer other detailed experimental description in the Supplementary Materials.

3. Results and discussion

3.1. Theoretical design of facet-dependent plasmonic photocatalysts

The model of bulk BiOBr is firstly constructed (Fig. 1a), with the (001) and (010) facets highlighted for surface cleavage and Bi metal deposition. Due to the BCA on the (001) facet, it is apparently deduced that there exists sole interaction in the interface between Bi metal and the (001) facet. As can be seen from the electronic localization function
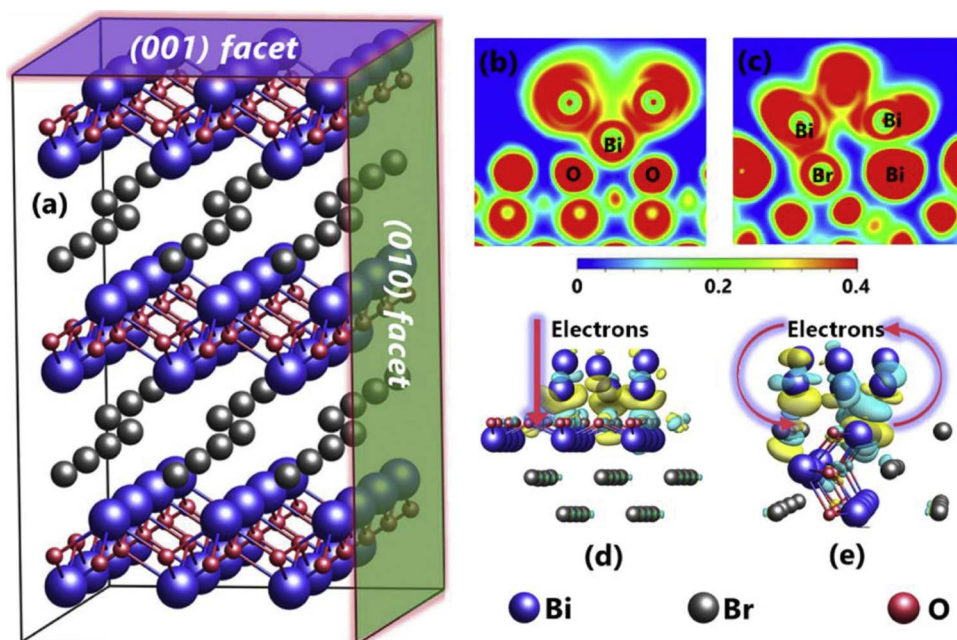
Fig. 1. Calculation model of BiOBr (a). Electron localization function (ELF) of Bi metal deposited at the (001) facet of BiOBr (Bi-001, b) and Bi metal deposited at the (010) facet of BiOBr (Bi-010, c). Charge density difference of Bi-001 (d) and Bi-010 (e). Electrons accumulation is in blue and depletion in yellow, respectively. The isosurfaces are set to 0.005 eV Å^{-3}. (For interpretation of the references to colour in this figure legend, the reader is referred to the web version of this article.)

(ELF, Fig. 1b) for Bi-001, the covalent bonding is generated between Bi metal and the surface terminated O atoms. On the contrary, Bi metal is bonded with both Bi and Br atoms on the (010) facet (Fig. 1c), which is caused by the SCA. It is well-accepted that the formation of covalent bonds originates from the oriented charge flow between two atoms. Thus the directions of interfacial charge transfer require further investigation.

Fig. 1d and e depict the charge density difference between Bi metal and the (001)/(010) facets, respectively. It is notable that an electrons transfer channel is established at the Bi-001 interface (Fig. 1d), which provides a high possibility for the SPR induced hot electrons to migrate from Bi metal to the O atoms on (001) facet. Hence the SPR effect of Bi metal *via* this transfer channel can be realized under light irradiation. However, the extra electrons that the (001) facet acquire may undergo undirectional motion on the surface, which consequently triggers inevitable charge recombination. Also, the rather weak van der Walls force between layers can severely impede the charge transfer within the bulk. For Bi-010, a covalent loop is evidently generated at the interface along the path of $[Bi_2O_2]^{2+} \rightarrow$ Bi metal $\rightarrow Br^-$, which contributes to electrons migration in a steered direction (Fig. 1e). The effective interfacial charge separation is dominantly dependent on the SCA of $[Bi_2O_2]^{2+}$ and Br^- on the (010) facet. Specifically, the electrons in the outer orbit of $[Bi_2O_2]^{2+}$ have a tendency to transfer to Bi metal. Then the obtained electrons of Bi metal migrate to Br^- along with the SPR hot electrons, confirming the fact that the ELF between Bi and Br^- is strengthened in comparison with that between Bi and $[Bi_2O_2]^{2+}$ (Fig. 1c). Thus it is expected that Bi-010 should manifest more efficient photocatalytic performance than that of Bi-001.

3.2. Photocatalysts fabrication

Inspired by the theoretical design, we fabricated the BiOBr with (001) and (010) facets exposure. Then Bi metal is deposited on BiOBr *via* the use of NaBH$_4$ as the reductant. The XRD patterns in Fig. 2a show the intensified diffraction peaks of (001) and (002), revealing the exposure of the (001) facet. With increasing the amount of NaBH$_4$, new characteristic peaks (27.2°, 38.2°, 39.3° and 49.5°) are detected, and gradually strengthened, attributed to Bi element (JCPDS card no. 05-0519). When the concentration of NaBH$_4$ was 30, 50, 70 and 90 mmol L^{-1}, using 001 as precursor material, the obtained samples were denoted as 001-30, 001-50, 001-70 and 001-90, respectively.

While for 010, the obtained samples were labeled as 010-30, 010-50, 010-70 and 010-90, respectively. Similar phenomenon is observed in the XRD patterns of the (010) facet exposed samples (Fig. 2b). It is also notable that the peaks of Bi in 010-30, 010-50, 010-70 and 010-90 are stronger than those in 001 with the same amount of NaBH$_4$ added, indicating that Bi^{3+} can be more effectively reduced to Bi^0 on the (010) facet than that of the (001) facet. This phenomenon originates from the SCA on the (010) facet, which results in the increased exposure of Bi atoms in comparison with that of the (001) facet, as the relaxed microstructures depict (Fig. S1). Moreover, the detailed elemental composition of the as-prepared samples was characterized by the XPS survey spectra (Fig. S2), which demonstrates that Bi, O and Br coexist in these samples. Two bands at approximately 159.8 and 165.0 eV ascribing to Bi 4f$_{7/2}$ and Bi 4f$_{5/2}$ can be observed in 001 and 010 samples (Fig. 2c and d) respectively, which are in agreement with those of BiOBr. [31,38] After the 20 nm sputtering of the 001-70 and 010-70, it is observed that the Bi^0 peaks can be detected with increased peak intensities, ascribed to the etching of the oxide film on Bi metal for more Bi^0 exposure (Fig. 2e and f). In addition, the snapshots of Bi deposition reaction at 001 and 010 (Fig. 2g) confirm that the surface of (010) facets exposes more Bi element than that of the (001) facet, leading to more rapid reduction of Bi^{3+} to Bi^0.

Morphologies of these samples are subsequently investigated by the scanning electron microscopy (SEM) images. The results show that the as-prepared 001 and 010 samples consist of nanosheet-shaped microstructures (Fig. S3a-S3b and Fig. S4a-S4b). The transmission electron microscopy (TEM) images further confirm the existence of nanosheets in 001 (Fig. S3d) and 010 (Fig. S4d). After inducement of Bi metal, the surface of 001-70 (Fig. S3c and S3e) and 010-70 (Fig. S4c and S4e) are densely covered with stacked Bi nanowires. High resolution TEM (HRTEM) images clearly demonstrate that two sets of lattice fringes are approximately 2.75 Å and 3.85 Å, respectively, being in agreement with the *d*-spacing of the (110) facet in the 001 sample (Fig. 3a) and (002) facet in the 010 sample (Fig. 3d). [31] After Bi metal deposition, the original lattice fringes of 001 and 010 samples are still observed. The emerging fringes can be assigned to (012) facet of Bi metal in 001-70 (Fig. 3b) and (110) facet of Bi metal in 010-70 (Fig. 3e), respectively. Single-crystal characteristics and the corresponding exposure of (001) facet (Fig. 3c) and (010) facet (Fig. 3f) are demonstrated by the corresponding selected-area electron diffraction (SAED) patterns. The angles between typical planes are in line with their respective theoretical
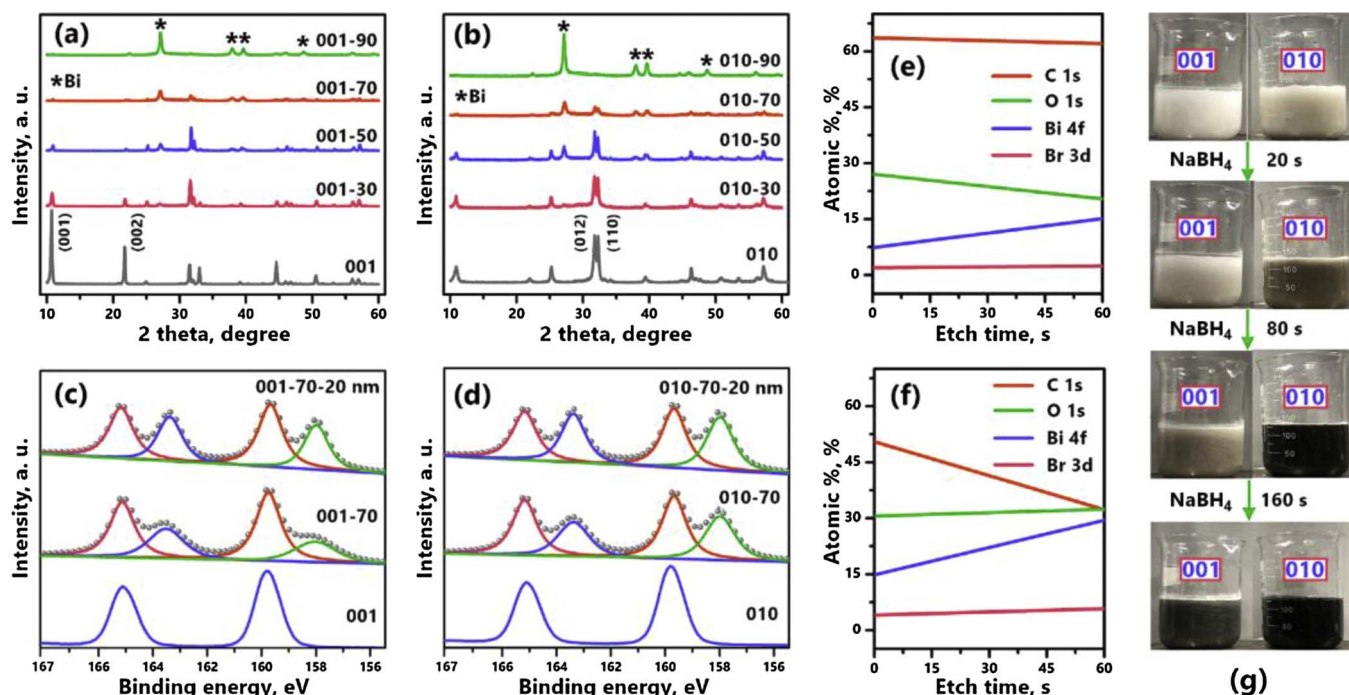
Fig. 2. XRD spectra of 001, 001-30, 001-50, 001-70 and 001-90 (a) and 010, 010-30, 010-50, 010-70 and 010-90 (b). XPS spectra (Bi 4f) of 001, 001-70 and 001-70-20 nm (sputtered 001-70 for 20 nm thickness of surface) (c) and 010, 010-70 and 010-70-20 nm (sputtered 010-70 for 20 nm thickness of surface) (d). Element content survey of 60 s' etching for 001-70 (e) and 010-70 (f). (g) Snapshots of Bi deposition reaction at 001 and 010 with added NaBH$_4$ for 160 s.

values.[39] Furthermore, the homogeneous dispersion of Bi, O, Br elements are verified *via* FESEM-EDX mappings, respectively for the 001 (Fig. S5) and 010 (Fig. S6) samples. In addition, increased specific surface area was observed after Bi deposition (Fig. S7), which may benefit the adsorption of the reactants and exposure of the active sites.

3.3. Photoactivity evaluation and photoelectrical property characterizations

The photocatalytic performance of the as-prepared samples is then investigated towards the NO removal under visible light irradiation. As shown in Fig. 4a, 001 and 010 samples exhibit inferior activities with NO removal ratios of *ca.* 4% and 14%, respectively. However, it is notable that the photocatalytic activity is significantly promoted when
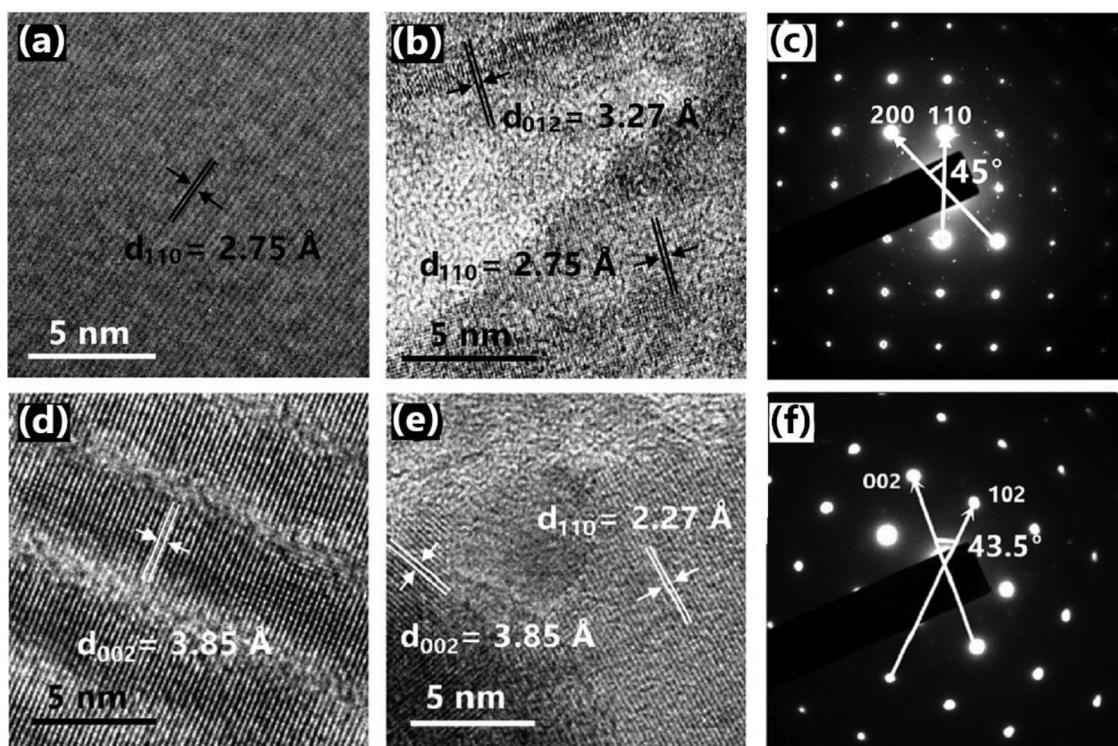

Fig. 3. HR-TEM images of 001 (a), 001-70 (b), 010 (d) and 010-70 (e). SAED patterns of 001 (c) and 010 (f).
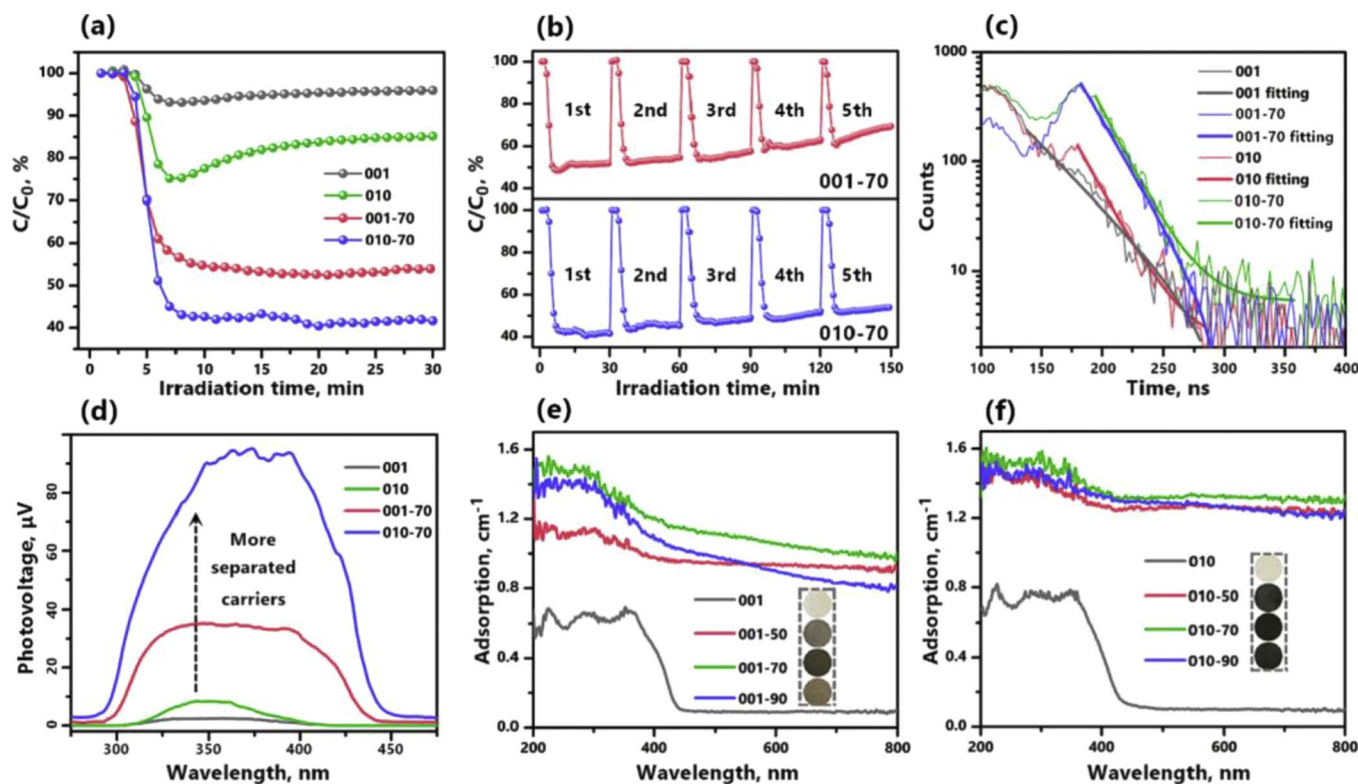
Fig. 4. Photocatalytic activity evaluation of 001, 010, 001-70 and 010-70. (a) photocatalytic cycling tests for 001-70 and 010-70. (b) ns-level time-resolved fluorescence spectra surveyed at room temperature (c) and surface photovoltage (SPV) spectra (d) for 001, 001-70, 010 and 010-70. UV–vis DRS spectra of 001, 001-50, 001-70 and 001-90 (e), 010, 010-50, 010-70, 010-90 (f). The insets of (e) and (f) are color comparison of different samples.

Bi metal is induced both for 001-70 and 010-70 (Fig. S8). The 010-70 demonstrates further enhanced visible light photocatalytic activity with NO removal ratio of 60.4% compared with 001-70 (50.1%). This result suggests that the introduction of plasmonic metal benefits 010-70 more than that of 001-70. Especially, the 010-70 also shows high durability during the cycling test. As depicted in Fig. 4b, 010-70 can be used repetitively for more than five times without obvious deactivation. On the contrary, the NO removal ratio of 001-70 undergoes a sharp reduction from 50.1% to 26.2%. Thus it is certified that Bi metal deposition benefits the (010) facet for the enhanced plasmonic photocatalytic efficiency of BiOBr, in comparison with that of the (001) facet. It is also worth mention that the optimized Bi-BiOBr shows the most outstanding performance among the commonly applied visible light photocatalysts in NO removal performance. (Table S1).

Moreover, photoelectrical properties of the as-prepared samples were investigated to reveal the mechanism for the enhancement of photocatalytic efficiency. It is demonstrated by PL spectra (Fig. S9) that the electron-hole recombination is indubitably inhibited. The ns-level time-resolved fluorescence decay spectra are employed to illustrate the charge motion dynamics with curves fitted *via* the Biexponential decay function (Fig. 4c). Obviously, in contrast to the pristine ones, the lifetime of charge carriers in 001-70 and 010-70 are prolonged, elucidating that the Bi deposition could effectively boost the charge transfer and separation. Therein, a further increase of the lifetime in 010-70 is detected compared to that of 001-70. This should be ascribed to the particular SCA on (010) facet, which benefits the interfacial charge separation more effectively, compared to the BCA on (001) facet, which certifies the theoretical calculations (Fig. 1). The surface photovoltage (SPV) spectra (Fig. 4d) show that 010-70 has a distinct extension to visible light than that of 001-70 and the bare ones.[40,41] Also, the significantly enhanced separated charge of the 010-70 sample clearly demonstrates that the interfacial charge separation is facilitated, owing to the newly-established route for interfacial charge transfer in Bi-010.

These photoelectrical properties indicate that the effective suppression of the interfacial charge carriers' recombination and fast transfer rate are conclusively responsible for the elevated photocatalytic activity of Bi-010. In addition, the UV–vis DRS spectra are measured to investigate the light absorption properties. As shown in Fig. 4e, the absorption of 001 sample is significantly intensified after Bi deposition and the color changes from light to dark (Fig. 5e inset). Similar results are observed in the 010 samples (Fig. 4f), which agrees well with the results of 001 samples.

Fig. 5 Low-temperature solid-state electron paramagnetic resonance (EPR) is employed to further investigate the nature of the change of light sensibility during the Bi deposition. As shown in Fig. 5a–d, under the visible light irradiation, these EPR signals are found to intensify in 001-70 and 010-70 respectively than 001 and 010, confirming that the plasmonic photocatalysts are more sensitive to light, and the charge mobility can be effectively promoted by Bi deposition. However, it could not be neglected that all these samples share a separate resonance approximately at g = 2.0, indicating the existence of the intrinsic oxygen vacancies (OVs) [42,43]. It is well-accepted that OVs are common and easily generated in general catalysts fabrication process [44,45], thus the function of OVs requires to be clarified. As the density of states (DOS) calculations represent (Fig. 6a–d), defect levels are detected in the middle of the band gap. Thus the charge transfer from the valence band (VB) to the conduction band (CB) is boosted by providing a foothold on the middle springboard, which leads to the intensified light absorption and agrees with the UV–vis DRS results (Fig. 4e and f). The O_2 activation on the different surfaces is then calculated (Fig. 6e–h). As expected, the O_2 molecules manifest stronger adsorption on OV-001 and OV-010 than those of the pristine ones, which indicates that the OVs are the primary active sites for O_2 activation. It is obvious that the adsorption energy (E_{ads}) and carried electrons (Δq) of O_2 on OV-010 are obviously higher than that of OV-001, which implies that the O_2 molecule receives more electrons and
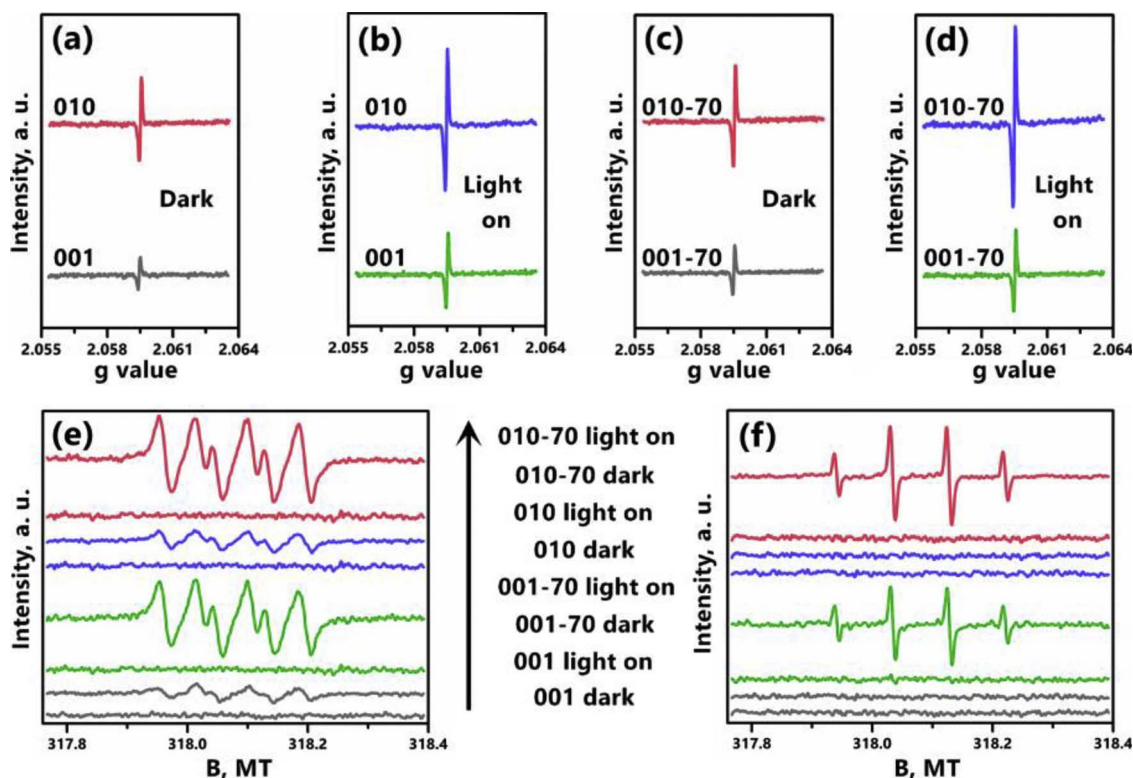
Fig. 5. EPR spectra of 001 and 010 in dark (a) and with visible-light on for 15 mins (b), 001-70 and 010-70 in dark (c) and with visible-light on (d). The scales of intensity are all taken from −400 to 2000 in (a)–(d). DMPO spin-trapping ESR spectra in methanol dispersion for DMPO-·O_2^- (e) and in aqueous dispersion for DMPO-·OH (f) of 001, 001-70, 010 and 010-70.
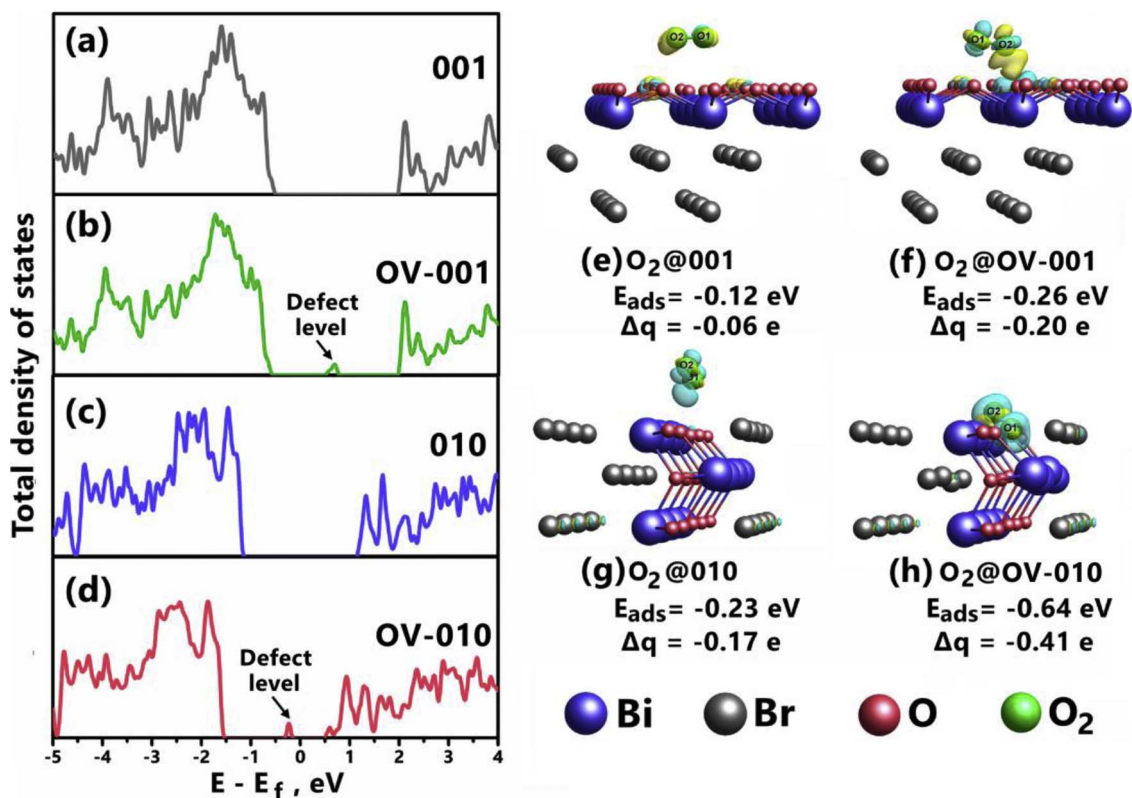

Fig. 6. Calculated total density of states (TDOS) for pristine surfaces and surfaces with oxygen vacancies (Ov) defects of 001 (a, b) and 010 (c, d); charge density difference of O_2 adsorption and activation at 001 (c), ov-001 (d), 010 (e) and ov-010 (f). Electrons accumulation is in blue and depletion in yellow, respectively. The isosurfaces are set to 0.003 eV Å^{-3}. E_{ads} and Δq depict the adsorption energy and carried electrons of O_2 molecules. Negative means heat release and electrons obtainment, respectively. (For interpretation of the references to colour in this figure legend, the reader is referred to the web version of this article.)

gets activated readily to $\cdot O_2^-$ on OV-010, in comparison with that of OV-001.

Fig. 6 The formation of active radicals is the prerequisite to general photo-oxidation reactions.[46–48] Hence the ROS is thus investigated by measuring the DMPO spin-trapping ESR spectra. Under visible light illumination, the intensities of four strong peaks in Fig. 5e, ascribed to O_2^-, are increased in the order of 001 < 010 < 001-70 < 010-70, consistent with the order of enhanced O_2 activiation (Fig. 6). Meanwhile, no signals of $\cdot OH$ are detected in the pristine 001 and 010 samples (Fig. 5f). After modification, the $\cdot OH$ species are observable under visible light excitation in 001-70 and 010-70. As the generation of $\cdot OH$ obeys the $\cdot O_2^- \rightarrow H_2O_2 \rightarrow \cdot OH$ route,[46,49] it is reasonable that the mass production of $\cdot O_2^-$ in 010-70 leads to more $\cdot OH$ formation than that of 001-70. These results support the theoretical calculations that the SCA induced interfacial charge separation in Bi-010 benefits the light-driven electrons generation, which are subsequently captured by the isolated O_2 molecules to form $\cdot O_2^-$ [50]. Then the $\cdot O_2^-$ species are transferred to $\cdot OH$. By taking advantage of the facet effect, the mass production of ROS in 010-70 leads to fruitful enhancement of the photocatalytic activity than those of 001-70 and the pristine ones.

### 3.4. Promotion mechanism of interfacial charge separation

The SPR effect of Bi metal is simulated with a rigorous Maxwell solver. The simulation model is set to three parallel Bi nanowires at topview (Fig. 7a) and sideview (Fig. 7b). A significant enhancement of the electric field intensity is observed in the vicinity of the nanowires, and in the contacting interfaces between two nanowires. Thus, the SPR effect of Bi metal is associated with the intensive local electric field. According to the theoretical and experimental results, a facet-dependent promotion mechanism of plasmonic photocatalysis on Bi-BiOBr is firstly proposed (Fig. 7c). As for a semiconductor, it is required that the electrons migrate from VB to CB, leaving holes at the VB, achieving the charge separation under light illumination. With the introduction of OVs, the electron transition is divided to two continuous paths (Path ① and Path ②), which endows electrons with easier access to hop from VB to CB, in comparison with the defect-free samples. As we demonstrated before (Fig. 1e), electrons transit along the pathway of $[Bi_2O_2]^{2+} \rightarrow Bi$ metal $\rightarrow Br^-$ at the interface of Bi-010. Assisted by deposited Bi metal, a distinctive transfer route (Path ③) is established at the (010) facet with SCA. However, the Path ③ is unfavorable for the Bi@001 sample. Then

the electrons that Bi metal obtained transfer along with the SPR hot electrons from Bi metal to the CB of BiOBr (Path ④). The facet effect dominantly leads to more electrons transition and much enhanced charge separation at Bi-010 than that of Bi-001. The effective charge separation in turn contributes to more effective production of the chemical reactive $\cdot O_2^-$ at CB (Path ⑤) and $\cdot OH$ at VB (Path ⑥) respectively, which is conclusively responsible for the significantly reinforced plasmonic photocatalytic efficiency of Bi-010.

On account of the success in plasmonic photocatalysts design in Bi-BiOBr system, we further validated the new interfacial charge separation and transfer pattern in other systems with alternative plasmonic metal and semiconductors, including Ag-BiOBr, Au-BiOBr, Bi-BiOCl and Bi-BiOI. Ag-BiOBr was firstly fabricated with the exposure of respective (001) and (010) facet (Fig. S10 and S11). Their light absorption properties (Fig. S12) and photocatalytic efficiency (Fig. S13) demonstrate similar results with that of Bi-BiOBr. Then the detailed interfacial charge separations in Ag-BiOBr (Fig. 8a–d) and Au-BiOBr (Fig. 8e–h) are revealed by DFT calculations, indicating highly consistent patterns with that of Bi-BiOBr. As for alternative semiconductors, the photocatalytic efficiency patterns are still maintained in Bi-BiOCl (Table S2). Also, theoretical results support the perspective that the SCA significantly benefits the interfacial charge separation in the plasmonic photocatalytic systems of Bi-BiOCl (Fig. 8i–l) and Bi-BiOI (Fig. 8m–p).

4. Conclusions

In summary, we clearly proposed and certified that the interfacial charge separation and transfer patterns of plasmonic photocatalysts are dependent on the charge alternation of the exposed semiconductor facets. This work provides direct evidences that the surface charge alternation marvelously benefits the interfacial charge separation of plasmonic photocatalysts *via* establishing a new transfer route between the two counterparts along the path of surface cation → plasmonic metal → anion, undoubtedly exceeding that of the bulk charge alternation. This particular pattern can lead to highly enhanced interfacial charge separation efficiency, light absorption ability, reactive oxygen species generation and photocatalysis efficiency. More efficient plasmonic photocatalysts can be designed by this facet-dependent protocol. The current understanding and perspective here can also open new possibilities for manipulating general facet effect in environmental, energy, materials and catalysis science.
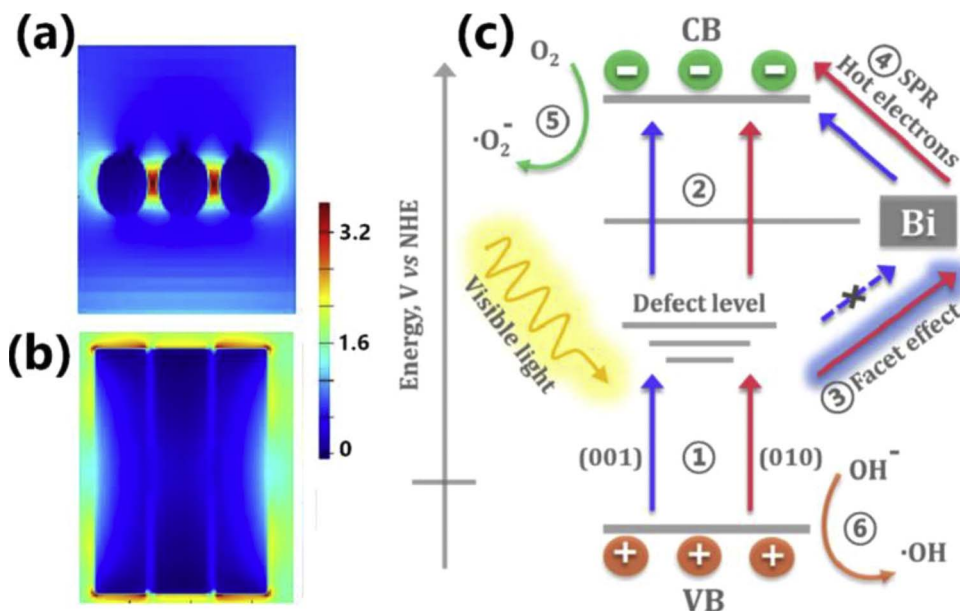
Fig. 7. SPR-induced local electromagnetic fields simulation in the Bi nanowires at sideview (a) and topview (b). The Bi nanowires are irradiated by plane waves light source with a wavelength of 420 nm that occur vertical to the presented plane. The scale bar shows the relative increase in field intensity. (c) Proposed visible photocatalysis mechanism of Bi@defective-BiOBr nanosheets with (001) and (010) facets exposure, respectively.
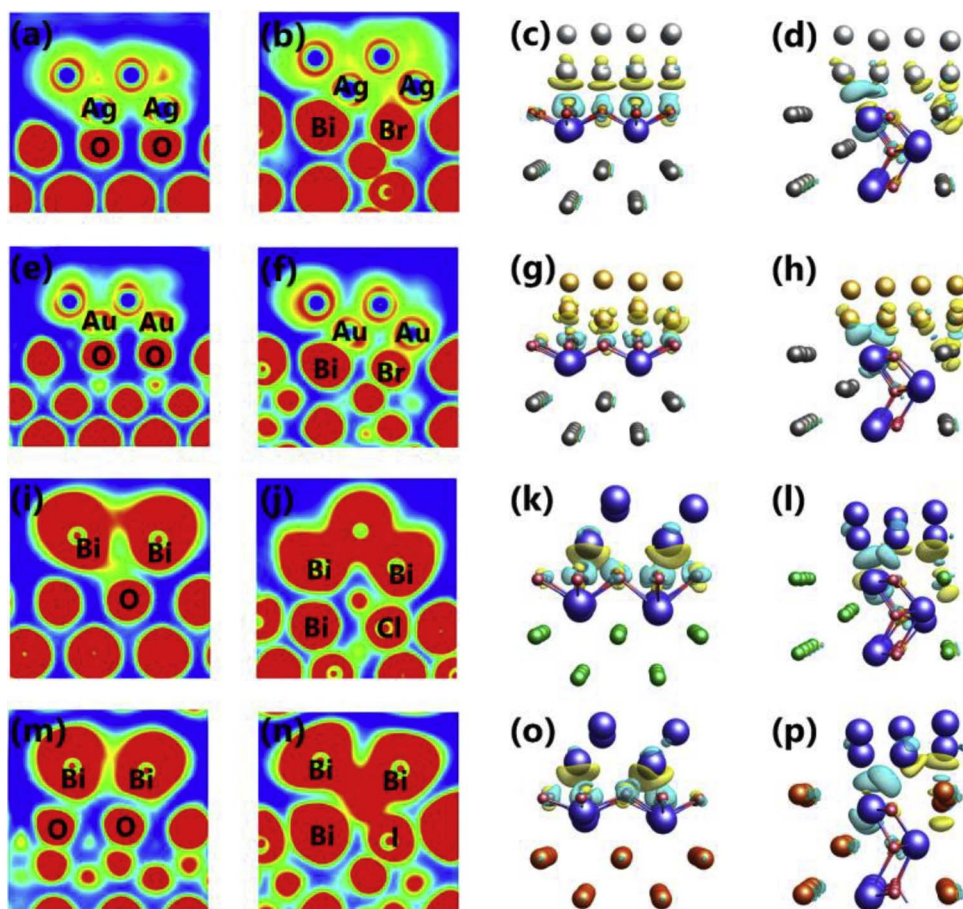
Fig. 8. Electron localization function (ELF) and charge density difference of Ag-BiOBr (a–d), Au-BiOBr (e–h), Bi-BiOCl (i–l) and Bi-BiOI (m–p). The ranges of ELF are all set to 0–0.5. silver, golden, blue, red, grey, green and orange spheres depict Ag, Au, Bi, O, Br, Cl and I atoms, respectively. Electrons accumulation is in blue and depletion in yellow, respectively. The isosurfaces are all set to 0.005 eV Å^{-3}. (For interpretation of the references to colour in this figure legend, the reader is referred to the web version of this article.)

Acknowledgments

Appendix A. Supplementary data

Supplementary data associated with this article can be found, in the online version, at https://doi.org/10.1016/j.apcatb.2017.12.057.

References

[1] S. Wang, Y. Gao, S. Miao, T. Liu, L. Mu, R. Li, F. Fan, C. Li, J. Am. Chem. Soc. 139 (2017) 11771–11778.
[2] C. Clavero, Nat. Photonics 8 (2014) 95.
[3] G. Jiang, X. Li, M. Lan, T. Shen, X. Lv, F. Dong, S. Zhang, Appl. Catal. B: Environ. 205 (2017) 532–540.
[4] S. Tiewcharoen, C. Warakulwit, V. Lapeyre, P. Garrigue, L. Fourier, C. Elissalde, S. Buffière, P. Legros, M. Gayot, J. Limtrakul, Angew. Chem. Int. Ed. 56 (2017) 11431–11435.
[5] X. Liang, P. Wang, M. Li, Q. Zhang, Z. Wang, Y. Dai, X. Zhang, Y. Liu, M.H. Whangbo, B. Huang, Appl. Catal. B-Environ. 220 (2017) 356–361.
[6] D. Tsukamoto, Y. Shiraishi, Y. Sugano, S. Ichikawa, S. Tanaka, T.J. Hirai, J. Am. Chem. Soc. 134 (2012) 6309.
[7] F. Dong, T. Xiong, S. Yan, H. Wang, Y. Sun, Y. Zhang, H. Huang, Z. Wu, J. Catal. 344 (2016) 401–410.
[8] Z. Ni, W. Zhang, G. Jiang, X. Wang, Z. Lu, Y. Sun, X. Li, Y. Zhang, F. Dong, Chin. J. Catal. 38 (2017) 1174–1183.
[9] X. Meng, L. Liu, S. Ouyang, H. Xu, D. Wang, N. Zhao, J. Ye, Adv. Mater. 28 (2016) 6781.
[10] X. Yu, F. Liu, J. Bi, B. Wang, S. Yang, Nano Energy 33 (2017) 469–475.
[11] S. Bai, J. Jiang, Q. Zhang, Y.J. Xiong, Chem. Soc. Rev. 44 (2015) 2893.
[12] X. Li, W. Zhang, W. Cui, Y. Sun, G. Jiang, Y. Zhang, H. Huang, F. Dong, Appl. Catal. B Environ. 221 (2018) 482–489.
[13] S. Bai, L. Wang, Z. Li, Y. Xiong, Adv. Sci. 4 (2017) 1600216.
[14] S. Bai, X. Li, Q. Kong, R. Long, C. Wang, J. Jiang, Y. Xiong, Adv. Mater. 27 (2015) 3444–3452.
[15] X.A. Dong, W. Zhang, W. Cui, Y. Sun, H. Huang, Z. Wu, F. Dong, Catal. Sci. Technol. 7 (2017) 1324–1332.
[16] H. Li, F. Qin, Z.P. Yang, X.M. Cui, J.F. Wang, L.Z. Zhang, J. Am. Chem. Soc. 139 (2017) 3513–3521.
[17] H. Wang, X. Lang, R. Hao, L. Guo, J. Li, L. Wang, X. Han, Nano Energy 19 (2016) 8–16.
[18] S. Linic, P. Christopher, D.B. Ingram, Nat. Mater. 10 (2011) 911–921.
[19] K. Zhao, L. Zhang, J. Wang, Q. Li, W. He, J.J. Yin, J. Am. Chem. Soc. 135 (2013) 15750–15753.
[20] W.J. Fang, Z. Jiang, L. Yu, H. Liu, W.F. Shangguan, C. Terashima, A. Fujishima, J. Catal. 352 (2017) 155–159.
[21] H. Wang, X. Yuan, Y. Wu, G. Zeng, W. Tu, C. Sheng, Y. Deng, F. Chen, W.C. Jia, Appl. Catal. B-Environ. 209 (2017) 543–553.
[22] J. Yu, J. Low, W. Xiao, P. Zhou, M. Jaroniec, J. Am. Chem. Soc. 136 (2014) 8839–8842.
[23] J. Li, K. Zhao, Y. Yu, L. Zhang, Adv. Funct. Mater. 25 (2015) 2189–2201.
[24] Y. Yan, S. Sun, Y. Song, X. Yan, W. Guan, X. Liu, W. Shi, ACS Nano 7 (2013) 2532–2540.
[25] J. Li, G.M. Zhan, Y. Yu, L. Zhang, Nat. Commun. 7 (2016) 11480.
[26] J. Li, H. Li, G. Zhan, L. Zhang, Acc. Chem. Res. 50 (2017) 112.
[27] C.Y. Wang, Y.J. Zhang, W.K. Wang, D.N. Pei, G.X. Huang, J.J. Chen, X. Zhang, H.Q. Yu, Appl. Catal. B-Environ. 221 (2017) 320–328.
[28] H. Li, J. Shang, Z. Ai, L. Zhang, J. Am. Chem. Soc. 137 (2015) 6393–6399.
[29] Q. Li, X. Zhao, J. Yang, C.J. Jia, Z. Jin, W. Fan, Nanoscale 7 (2015) 18971.
[30] H. Li, T. Hu, N. Du, R. Zhang, J. Liu, W. Hou, Appl. Catal. B-Environ. 187 (2016) 342–349.
[31] X. Wu, H.N. Yun, L. Wang, Y. Du, S.X. Dou, R. Amal, J. Scott, J. Mater. Chem. A 5 (2017) 8117–8124.
[32] R.B. Wang, B.X. Li, C.H. Fang, J.F. Wang, Adv. Mater. 26 (2014) 5274–5309.
[33] J.P. Perdew, K. Burke, M. Ernzerhof, Phys. Rev. Lett. 77 (1996) 3865.
[34] G. Kresse, J. Furthmuller, Comput. Mater. Sci. 6 (1996) 15–50.
[35] T. Weiland, AEU-Int. J. Electron. C 31 (1977) 116–120.
[36] S. Yan, J. Krantz, K. Forberich, C. Pflaum, C.J. Brabec, J. Appl. Phys. 115 (2013)

154303.

[37] Q. Zhao, T. Xie, L. Peng, Y. Lin, P. Wang, L. Peng, D. Wang, J. Phys. Chem. C 111 (2013) 17136–17145.

[38] F. Dong, T. Xiong, Y. Sun, H. Huang, Z. Wu, J. Mater. Chem. A 3 (2015) 18466–18474.

[39] J. Jiang, K. Zhao, X. Xiao, L. Zhang, J. Am. Chem. Soc. 43 (2012) 4473–4476.

[40] D. Xu, T. Jiang, D. Wang, L. Chen, L. Zhang, Z. Fu, L. Wang, T. Xie, ACS Appl. Mater. Interfaces 6 (2014) 9321.

[41] X. Zhang, L. Zhang, T. Xie, D. Wang, J. Phys. Chem. C 113 (2009) 7371–7378.

[42] J. Li, Y. Yu, L. Zhang, Nanoscale 6 (2014) 8473.

[43] T. Xia, Y. Zhang, J. Murowchick, X. Chen, Catal. Today 225 (2014) 2–9.

[44] J. Nowotny, M.A. Alim, T. Bak, M.A. Idris, M. Ionescu, K. Prince, M.Z. Sahdan, K. Sopian, M.A. Mat, W. Sigmund, Chem. Soc. Rev. 44 (2015) 8424–8442.

[45] V. Gurylev, C.Y. Su, T.P. Perng, J. Catal. 330 (2015) 177–186.

[46] Y. Nosaka, A.Y. Nosaka, Chem. Rev. 117 (2017) 11302–11336.

[47] J. Li, W. Cui, Y. Sun, Y. Chu, W. Cen, F. Dong, J. Mater. Chem. A 5 (2017) 9358.

[48] A. Kudo, Y. Miseki, Chem. Soc. Rev. 38 (2009) 253–278.

[49] F. Dong, Z. Wang, Y. Li, W.K. Ho, S.C. Lee, Environ. Sci. Technol. 48 (2014) 10345–10353.

[50] S. Selcuk, A. Selloni, Nat. Mater. 15 (2016) 1107.